Ductile damage and fragmentation of highly porous gamma-alumina under multi-point crushing

Vincent Le Corre, Lina Jolivet, Soline Mathevet, Carole Bobin, Meille Sylvain

To cite this version:

Vincent Le Corre, Lina Jolivet, Soline Mathevet, Carole Bobin, Meille Sylvain. Ductile damage and fragmentation of highly porous gamma-alumina under multi-point crushing. Ceramics International, 2020, 46 (16), pp.25584-25592. 10.1016/j.ceramint.2020.07.030 . hal-03002067

HAL Id: hal-03002067
https://ifp.hal.science/hal-03002067

Submitted on 12 Nov 2020

Title : **Ductile damage and fragmentation of highly porous γ-alumina under multi-point crushing test**

Authors : LE CORRE Vincent[1]*, JOLIVET Lina[1,2], MATHEVET Soline[1,2], BOBIN Carole[1], MEILLE Sylvain[2]
1: IFP Energies nouvelles, Rond-point de l'échangeur de Solaize, BP 3, 69360 Solaize, France
2: INSA de Lyon, Laboratoire MATEIS, 7, avenue Jean Capelle, 69621 Villeurbanne, France
* : corresponding author, @: vincent.le-corre@ifpen.fr , Tel : +33 437 702 306

Highlights :

- The multi-point crushing test reveals a damageable behavior of highly porous alumina used as catalyst supports
- Plastic deformation, micro-cracking and fragmentation are observed under multi-point crushing tests.
- The ductile damage of mesoporous γ-alumina can be represented by a Drucker-Prager plastic criterion

Graphical abstract:

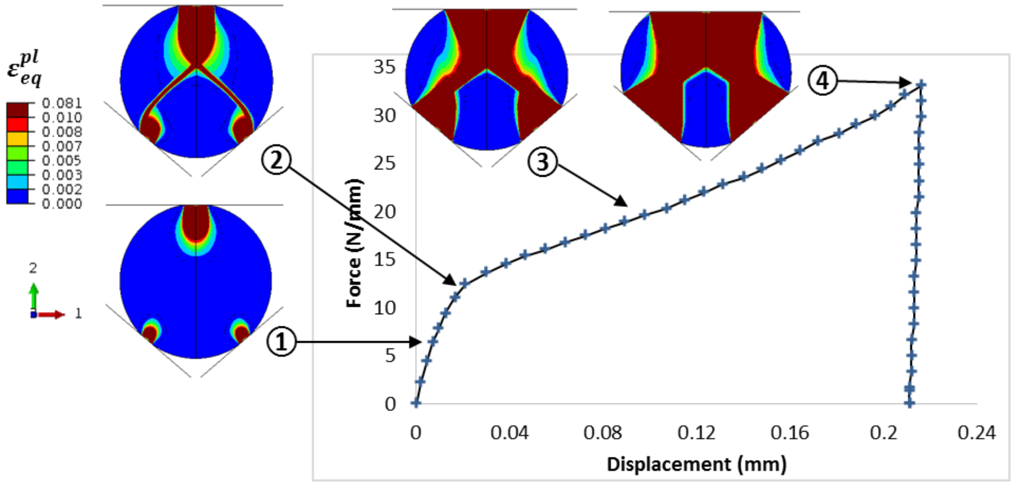

Keywords: Porous ceramics, yield strength, fragmentation pattern, fractography, Finite Element model, Drucker-Prager criterion

Abstract:

Mechanical behavior of highly porous alumina catalytic supports is investigated through a non-conventional approach consisting in a multi-point crushing of individual cylindrical extrudates. A ductile behavior characterized by irreversible deformation and fragmentation phenomena is observed and pointed out by experimental load-displacement curves. SEM fractographies of the fragments collected after the tests confirm the presence of dense micro-cracking and of local deformations under contact zones. A Finite Element analysis of the test shows that a Drucker-Prager strength criterion associated with a perfectly plastic flow rule mimics the global damageable behavior of the specimen under the multi-point crushing test. A correlation is proposed between the evolution of the mass of fine fragments and the plastic energy dissipation.

1 Introduction

Numerous petroleum refining processes require solid catalysts carried on a porous ceramic in fixed bed reactors. In such reactors, catalysts are immobile with respect to a fixed reference frame and oil flows through several horizontal catalysts beds. Mesoporous alumina are used as catalyst supports in hydrotreatment processes at high temperature and high hydrogen pressure [1]. Textural characteristics of these solids are specified by the nature of the process and are adjusted during preparation steps. Hydrotreatment catalysts exhibit a porosity fraction higher than 65% and a specific surface higher than 200 m^2/g to obtain high catalytic performance. Adequate mechanical strength is also required to ensure mechanical stability during catalyst preparation process, transport and all along in-service life. Particularly, formation of fragments may cause serious issues, such as pipe obstruction, uneven distributions of fluid flow and heat flux, high pressure drop across the reactor, and ultimately, significant yield losses. Not only the economic consequences are concerning [2], but particles production is also threatening the environment by the release of fine particles into the atmosphere. Standard test methods, like for determination of bulk crush strength of catalyst beds [3], give an insight of the risk of fragmentation of the material and assist selection of best formulations. However, catalysts development efforts remain mainly driven by catalytic performance and the mechanical strength of resulting solids is often undergone or optimized afterward. Therefore, a better understanding of the fragmentation process of catalytic supports is crucial to process supports with improved usage properties and to better assess fragmentation risk in-service.

Brittle behavior of porous catalytic supports under tensile stress has been extensively described [4–6]. Under tensile stress the material behaves like dense ceramics [7] and follows Griffith theory of brittle fracture [8,9]: a crack suddenly propagates from a critical flaw, leading to the fracture of the material. The most commonly used test to characterize the tensile strength of catalytic support is the side crushing test, also known as Brazilian test [10]. This standard method consists in a diametral compression of the specimen between parallel rigid plates, up to brittle fracture. For perfectly brittle materials, a tensile strength can be calculated. However, the non-perfect cylindrical shape of extruded supports, due to the drying and calcination processes, complicates the interpretation of the test. As damageable behavior in porous ceramics is favored by high porosity rates [11,12], brittle fracture sometime is never observed and the determination of the tensile strength is no more possible. For this reason, the three-points bending test has been proposed to measure the tensile strength of brittle supports [5,13,14]. The bending strength of extrudates was recently used by Beeckman et al. [15] to predict the reduction in the aspect ratio of extrudates due to brittle fractures in a fixed bed.

More recently, local damageable behavior of highly porous alumina under compression has been highlighted by Staub *et al.* [16] using spherical indentation, inspired by works of Lawn [17] and Clement *et al* [18]. Densification, micro-cracking and frictional sliding between γ alumina nano-crystallites agglomerates were suspected. A Drucker-Prager plasticity model [19] was successfully used to represent the material behavior under indentation. Damage is favored under multi-axial compressive loads producing high triaxiality stress states because unstable macro crack propagation is unlikely triggered. The spherical indentation test brings valuable information to understand fracture mechanisms at local scales. It is also especially convenient with small specimens such as catalyst extrudates. In order to investigate if ductile damage can occur at a larger scale to produce significant volumes of fragments, mechanical tests have to be conducted on entire extrudates. The aim of this paper is to enlighten quasi-ductile phenomena in highly porous catalytic supports by the mean of multiaxial crushing test on cylindrical extrudates. On a given sample of extrudates, both brittle or ductile fracture can be observed under the classic Brazilian test. What is more, the proportion of brittle or ductile fracture varies with material formulation, porosity fraction and possibly relative humidity. The motivation of the multi-points crushing is to favor ductile fracture thanks to a high stress triaxiality. The test is thus dedicated to ductile damage and fragmentation observation. It is complementary to the Brazilian test. However, it does not aim at representing the complex in-service conditions. The capacity of this test to trigger ductile damage has already been highlighted, for instance on concrete specimens by Artoni *et al.* [20]. Next chapter presents materials and experimental methods used in this work. Then a numerical interpretation of the multipoint crushing test is proposed. Simulation of local fragmentation of the samples requires advanced numerical tools, like intrinsic cohesive zone models [21,22], extended FE models (XFEM) with branching and friction [23,24], or Discrete Element models (DEM) as proposed in [25] or [26]. Because catalytic processes involve granular flows, we aim at introducing fragmentation in a DEM approach in a close future. However, a macroscopic continuous approach is preferred at a first stage. A Drucker-Prager plasticity model is identified from the experimental load-displacement curve. Experimental and numerical results are compared and discussed. Particularly, the ability of the plastic model to represent quasi-ductile behavior induced by local damage is discussed.

2 Materials and methods

2.1 Porous γ-alumina samples

The samples are cylindrical extrudates of γ-alumina, supplied by IFP Energies nouvelles (Solaize, France). The preparation process starts with the synthesis of boehmite [27,28] by precipitation of aluminum salts, washing with deionized water, and drying. Boehmite powder is kneaded by an acid solution to disperse boehmite aggregates, then neutralized with a basic solution. The paste is extruded through a cylindrical die, then dried and calcined at 540°C. The final diameter of extrudates is around 1.3 mm and their length varied from 3 to 6 mm. Two lots of extrudates are prepared. The porosity characteristics of each alumina, as determined by mercury intrusion porosimetry and nitrogen adsorption(BET specific surface area), are detailed in Table 1. The material displays a porosity fraction close to 70% with a unique population of pores centered close to 10 nm (mesopores).

Table 1: Characteristics of porous gamma alumina of the study

Alumina	Porous volume (mL/g) (1)	Pores median interconnection size (nm) (1)	Grain density (g/mL) (1)	BET specific surface area (m^2/g) (2)	Porosity rate (3)
#1	$0.81^{\pm0.01}$	11.7	$0.78^{\pm0.05}$	$303^{\pm14}$	$75\%^{\pm1\%}$
#2	$0.66^{\pm0.01}$	9.5	$0.99^{\pm0.05}$	$303^{\pm14}$	$69\%^{\pm1\%}$

(1) from mercury intrusion porosimetry
(2) from nitrogen adsorption
(3) from ratio of grain density to dense alumina density, considering ρ_{Al2O3}=3.2 g/mL

2.1 Multipoint crushing test

The multipoint crushing test consists in applying a compressive load on an extrudate placed on a V-shaped groove (Figure 1). The V-groove forms an angle of 40 degrees with the horizontal platen. Alternatively other angles can be used, from 20 deg to 60 deg. This configuration leads to a multi-axial compression of the sample. The mechanical testing device was an MTS-INSIGHT 1.0 (MTS Systems Corporation, USA) (Figure 2). The sample was compressed progressively up to a maximum crushing displacement after contact detection, then unloaded. Load and unload cycles were carried out at a constant speed of 0.12 mm/min. Two series of tests were conducted on 50 specimens on the first lot of extrudates: short tests and long tests, both with a groove angle of 40 deg. The maximum displacement was 0.15 mm for short tests and 0.35 mm for long tests. In case of sudden load drop larger than 5 N, the test automatically stopped. Applied load and crushing displacement were recorded at a frequency of 10Hz in order to detect such brittle events. In every test, the crushed sample and all fragments generated were collected. The material was sieved during 20 s at 70 Hz to select fine fragments smaller than 425 µm. Then, the sieved residue was sieved again to select coarse fragments under 850 µm.

Five series of tests of 10 specimens each have been conducted on the second lot of extrudates with grooves angles of 20, 30, 40, 50, and 60 deg.

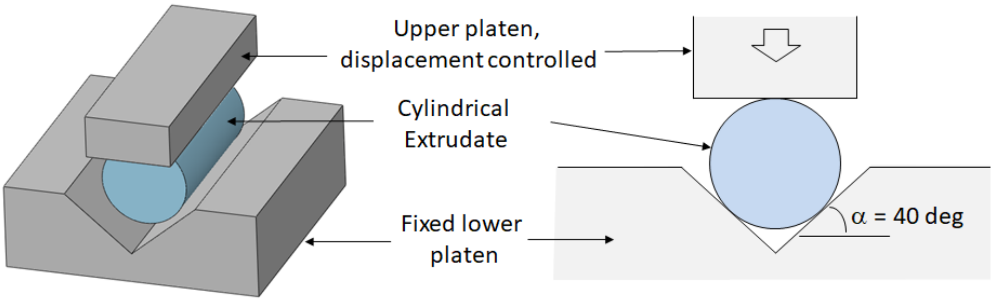

Figure 1: 3D and 2D diagrams of the multipoint crushing test on a cylindrical sample groove angle of 40 deg. The upper platen moves at constant velocity.

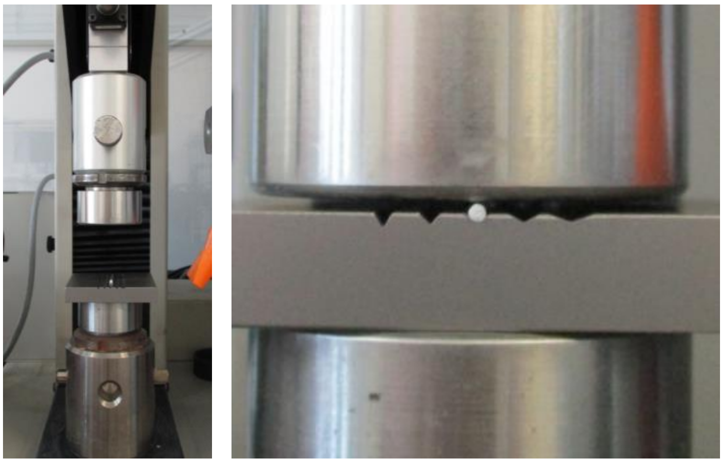

Figure 2: Set up of the multipoint crushing test of a cylindrical specimen

2.2 Granulometry of fragments

The size distribution of fine and coarse fragments (between 0.05 and 425 µm for fine ones and between 450 and 850 for coarse ones) were measured by a Mastersizer 3000 granulometer (Malvern Panalytical, UK). The particles are dragged by an air flow in front of a monochromatic laser beam. The light is scattered by the powder with various angles and intensities, according to the size of the particles (the bigger the particle, the smaller the diffraction angle). The analysis technique is based on Fraunhofer diffraction model, which approximates the particles to non-porous spheres and considers that particles are much larger than the light wavelength (approx. >10 µm). Moreover, diffraction angle is small (only near forward scattering is considered). A photodiode records the intensities and angles of the diffracted light and the device returns the size distribution of the particles. Surface and volume of particles are estimated assuming particles are spherical.

2.3 Scanning electron microscopy

The observation of the fracture surfaces of the largest fragments was carried out with a SEM Supra 40 (Zeiss, Germany). In order to observe the topographical contrast, the secondary electrons mode was used with an acceleration tension of 2 kV and magnifications from x30 to x250. Samples were glued on the holder with conductive double-sided carbon adhesive tape.

2.4 Numerical methods

2.4.1 Finite Element (FE) model

An FE model of the multipoint crushing test is build using the finite element package ABAQUS® [29]. The aim of the simulation is to assess the ability of the Drucker-Prager plastic model to represent ductile damage of highly porous γ-alumina support. As the ratio of the sample length over the sample diameter is higher than four, the stress state is poorly affected by the length of the support. The analysis is thus performed with a 2D plane strain model. Owing to the vertical plane of symmetry, only one half of the disc is analyzed. The platens are assumed to be rigid, hence the two-dimensional 2-node rigid element (R2D2) is used. The extrudate is meshed with quadratic eight-node plane strain elements (CPE8). The normal contact between the extrudate and the platens is constrained by a penalty stiffness between surfaces and solved by enforcing contact conditions in an average sense over regions nearby slave nodes rather than only at individual slave nodes. Thanks to the performance of this method, the mesh convergence is achieved with the mesh shown in Figure 3. A characteristic element size of around 15 µm is used, for a total number of element of 3250. The friction coefficient has very low impact on the simulation results. A Coulomb friction model is used with friction coefficient of 0.2 (low range estimation). A static calculation is performed, i.e., without any inertia effect, with the hypothesis of large displacements and deformations. The boundary conditions includes the symmetry condition on the vertical axis and the clamp of the lower platen. The first load step consists in imposing a vertical displacement of the upper platen up to the experimental maximum crushing displacement. The second load step consists in relaxing the crushing force. The mesh and boundary conditions are shown in Figure 3.

2.4.2 Material behavior, parameters

The material is assumed to present a macroscopic elastic-plastic behavior under compression. The Young modulus is 5.7 GPa, as determined by Staub from 3-points-bending tests [13]. A Poisson's ratio of 0.2 is used. According to experimental results on porous metallic oxides [30] and theoretical homogenization results on polycrystals [31], this value is appropriate for ceramics with a porosity rate of 70%. Works of Staub et al. [16] have shown that the mesoporous γ-alumina supports obey a ductile damageable behavior under spherical indentation, likely produced by nucleation and growth of micro-cracks and by frictional sliding of the micro-crack surfaces. Plasticity was used to represent local ductile behavior and a Drucker-Prager criterion was identified. A similar approach is used here in order to assess its validity at a larger scale. The plastic behavior of the solid is characterized by a Drucker-Prager yield surface:

$$\sigma_{\mathrm{eq}} + \tan\beta \cdot \sigma_{\mathrm{m}} - \left(1 - \frac{1}{3}\tan\beta\right) \cdot \sigma_{\mathrm{c}} = 0 \qquad \textbf{Eq. 1}$$

where σ_{m} is the mean stress of the Cauchy stress tensor $\boldsymbol{\sigma}$: $\sigma_{\mathrm{m}} = \frac{1}{3}\mathrm{tr}(\boldsymbol{\sigma})$, σ_{eq} is the equivalent von Mises stress: $\sigma_{\mathrm{eq}} = \sqrt{\frac{3}{2}.\mathbf{s}:\mathbf{s}}$, with $\mathbf{s}$ the deviatoric stress tensor : $\mathbf{s} = \boldsymbol{\sigma} - \sigma_{\mathrm{m}}.\mathbf{I}$ and $\mathbf{I}$ the 2nd order identity tensor, β is the internal friction angle and σ_{c} is the yield strength under compression of the material. A purely shearing plastic flow is assumed (no volumic dilatance) with perfect plasticity (no hardening).

The internal friction angle β and the compressive yield strength σ_{c} are parameters to be adjusted on experimental results. A first set of simulations is carried out with β values from 10 deg to 40 deg every 5 deg and σ_{c} values from 5 MPa to 35 MPa every 5 MPa (total of 49 simulations). The best combination of parameters is determined by comparing numerical force-displacement curve with experimental data. A second set of simulations is then run with a finer grid around this best combination to improve the correlation with experimental results (less than 10 simulations). The identification method is also applied to the second lot of extrudates tested on the groove at 40 deg. As a validation, simulations are compared with experimental results with other groove angles.

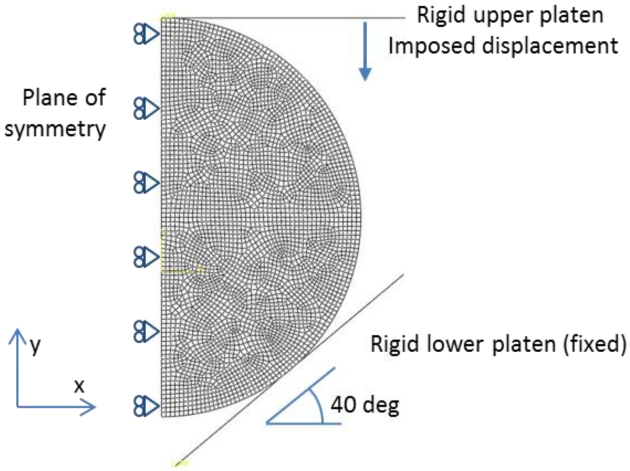

Figure 3: Finite element mesh employed for the simulation of the multipoint crushing test

3 Results and discussion

3.1 Experimental observations

3.1.1 Load-displacement curve

Figure 4a shows typical load-displacement curves obtained under multipoint crushing test. The crushing force is normalized by the samples lengths to take into account the individual variation in length of the samples. Several stages can be distinguished on the experimental curve. The initial stiffness at contact is very low. Impact of surface roughness is suspected and will be discussed in the next section. Next, the stiffness progressively increases as the contact surface between the specimen and the platens increases. Then the curve presents an inflection point: the apparent stiffness progressively decreases. Brittle events like load-drops are also observed. After unloading, an irreversible displacement is noted, larger for long tests as compared with short tests. These phenomena testify the progressive damage in the specimen, illustrating the quasi-plastic behavior of the material. Figure 4b presents the experimental dispersion of the experimental load-displacement curves for long tests. A mean load deflection, or characteristic failure load, can be estimated around 14 N/mm, with a standard deviation of 3 N/mm. A hardening behavior is obtained up to the maximal displacement. The apparent hardening stiffness increases for a displacement larger than 0.12 mm. Densification may be suspected, as observed on highly porous materials under multi-axial compression [18,32]. Large brittle events are mainly responsible for the dispersion of the normalized force.

Similar load-displacement curves are observed on the second lot of extrudates with groove angles from 20 deg to 60 deg. However, brittle fracture is obtained on a fraction of the extrudates tested at 20 deg and, to a lesser extent, at 30 deg. The impact of the groove angle on the characteristic failure loads is illustrated in Figure 9 : in agreement with the conclusion of [33], the higher the angle, the higher the mean failure load of the extrudate. The dispersion of the experimental mean failure load increases at angles of 50 deg and 60 deg. The angle of 40 deg therefore appears to be the optimal angle for the study of ductile damage of the supports.

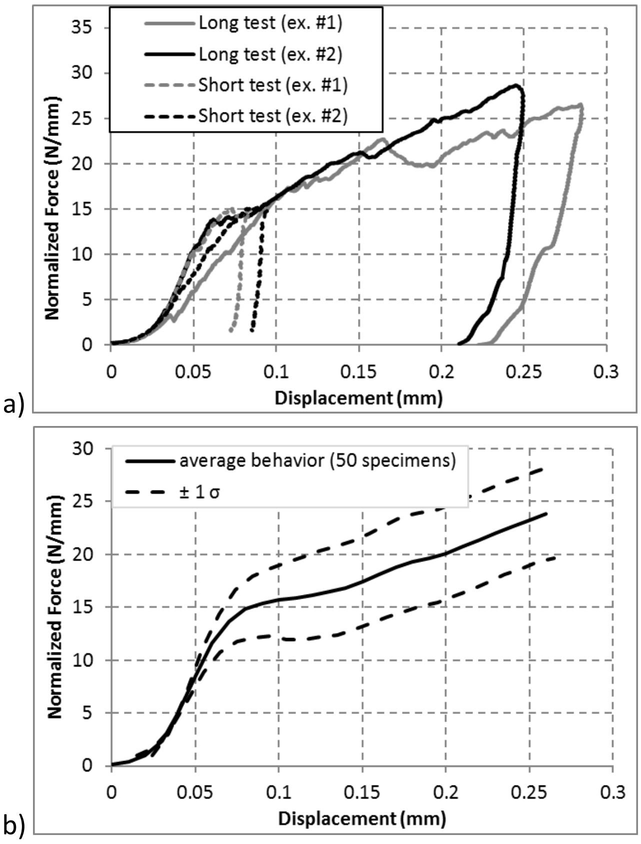

Figure 4: Experimental results
a) Typical load-displacement curves obtained under multipoint crushing
b) average behavior and standard deviation of load-displacement curve over 50 specimens (long test)

3.1.2 SEM Fractography

The majority of fracture patterns are as illustrated in Figure 5. More than 80% of specimens show at least one facture surface joining upper and lower contact areas. The external fragments are the largest and were selected for SEM observation. The core of the specimens is mainly turned into smaller fragments. Figure 6 shows typical images of the main fracture surfaces. Numerous micro-cracks are visible, the fracture surface is very irregular. The area close to the contact surface often shows more micro-cracks than the core area. Numerous fragments can be observed, they are likely still attached to the main fragment (Figure 6c). The deformation of the solid close to the contact zone is also highlighted: the contact surface of the cylindrical specimen is flattened with a compacted zone of approximately 100 µm thick (Figure 6a and b). These observations thus shows that the damage mechanism by micro-cracking both acts in the core of the specimen and under the surface of contact with the platens. It produces fragments and macro-deformation.

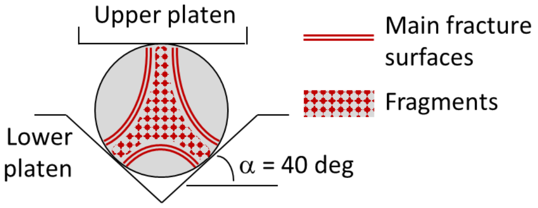

Figure 5: Scheme of the fracture pattern showing the main fracture surfaces, and the location of the zones generating fine fragments and external large fragments

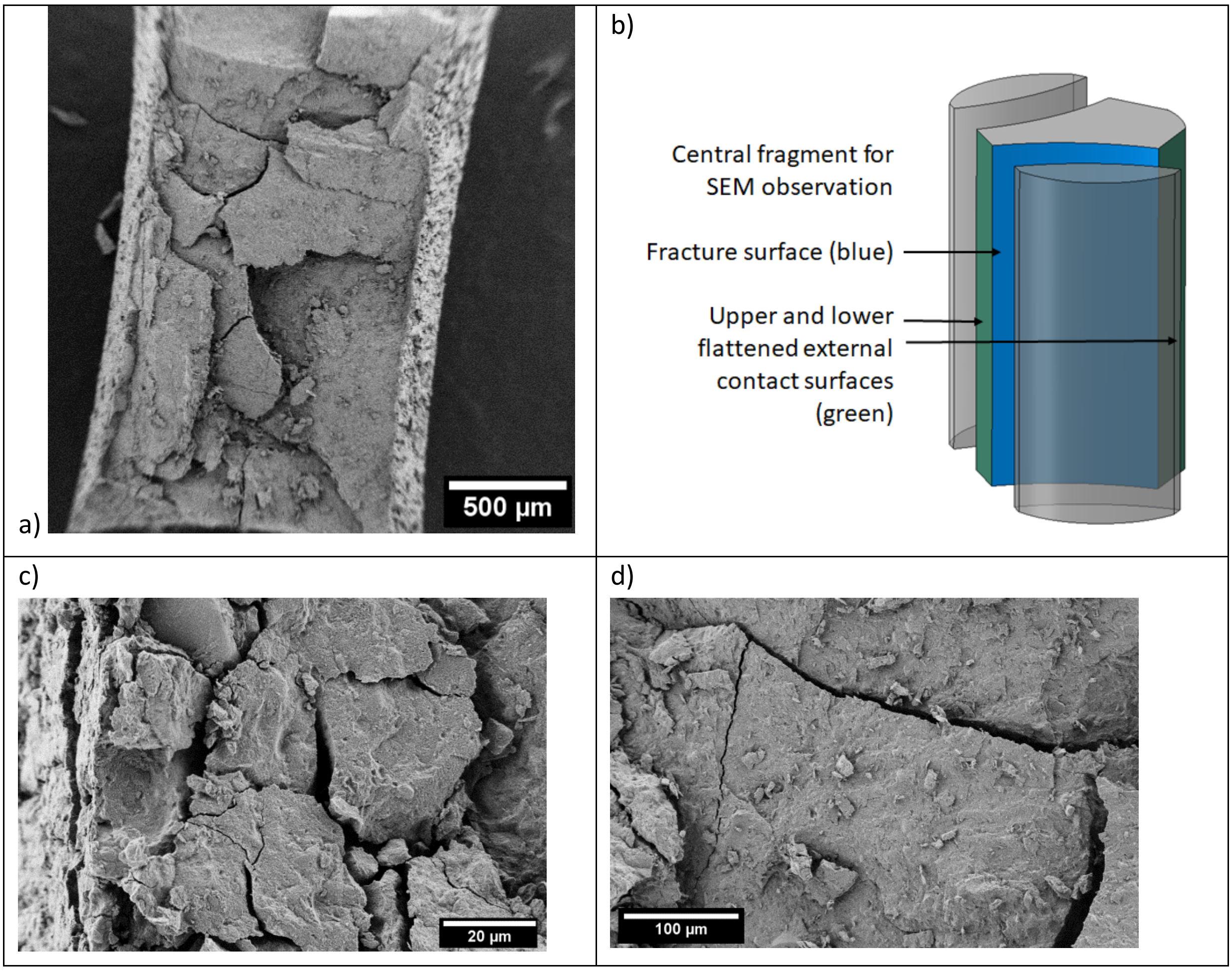

Figure 6: SEM fractography of a fragment
a) entire fragment: Numerous cracks are noted, the fracture surface is very irregular
b) Scheme of the fragment c) magnification on left side of the fragment, the flattened contact surface is visible
d) magnification on center of the fragment.

3.1.1 Total mass and mean size of fragments

Table 2 gathers information on the geometry and mass of fragments after sieving and granulometry measurements. For the short test series, masses of fine and coarse fragments respectively represent 2.3% and 8.7% of the initial mass of specimens. After the long test series, masses of fine and coarse fragments respectively represent 27.2% and 30.8% of the initial mass of specimens. The ratio of fine fragments strongly increases after long test i.e., for higher energy dissipation. The evolution of the fragments size confirms this trend: the volumic median diameter – i.e. the diameter splitting the distribution of fragments in two populations of equal cumulated volumes – decreases after long test. The high mass fraction of fragments represents a very large surface. The energy dissipated during the test, calculated from the area under the load-displacement curves, is also reported in Table 2. Energy dissipation is about 10 times higher in the long test as compared with the short test. The fracture surface is the sum of the areas of the internal cracks. Since each crack produces two surfaces, the crack surface is estimated as half the fragments surfaces. Numerous internal cracks have propagated without producing fragments, so the true total fracture surface is higher than this estimation. The ratio of the dissipated energy to the fracture surface is then estimated to 12.4 J/m². This value is higher, by a factor 2.4, than the critical energy release rate G_{IC} = 5.0 J/m² determined in [34] with 3-points-bending tests on notched specimens. Energy is obviously dissipated by internal frictional mechanisms, not only by brittle propagation of cracks.

Table 2: Fine and coarse fragments collected after the multipoint crushing tests

Test series	Initial mass (Total of 50 specimens) (mg)	Total dissipated energy (mJ)	Fine fragments < 425 µm			Coarse Fragments < 850 µm		
			Mass (mg) (% of initial)	Volumic median diameter (µm)	Surface (mm²)	Mass (mg) (% of initial)	Volumic median diameter (µm)	Surface (mm²)
short test	218	89	5.1 (2.3%)	240	253	19 (8.7%)	631	342
long test	232	834	63.2 (27.2%)	7	132 076	71.5 (30.8%)	478	1 966

3.2 Numerical results

3.2.1 Drucker-Prager criterion identification

The nonlinear macroscopic behavior of the extrudates under the multi-points crushing test is estimated by FE simulation using a Drucker-Prager constitutive law. Figure 7 shows how the internal friction angle β and the yield strength under compression σ_c impact the loading phase of the load-displacement curve. Two stages can be distinguished: the apparent stiffness progressively decreases up to a global yielding load, then a hardening is observed. As a perfectly plastic flow rule is used in the constitutive law, the apparent hardening may be due to the geometrical effect of large deformations. The yield stress influences not only the global yielding load but the stiffness at early stage. A rather limited influence of the friction angle is also pointed out: the apparent hardening stiffness slightly increases with the friction angle (see Figure 7b).

The numerical curves illustrated in Figure 7, show strong similarities with the experimental behavior shown in Figure 4: an apparent stiffness reduction at early stage followed by a global yielding, and a linear hardening. Notable differences are also pointed out. The initial elastic stiffness is high in the simulation whereas the experimental stiffness increases slowly at low loads. SEM pictures (Figure 6) shows that the contact surface is flatten compared with initial surface. Surface roughness can thus entail a displacement of few micrometers before stabilizing contact. Moreover, the average experimental stiffness at unloading is also lower than the numerical stiffness. The Young modulus of the material is not questioned since its value has been confirmed by several other tests. The low experimental unloading stiffness is evenly observed on short and long tests, so it is not an impact of damage in the sample. The additional compliance is likely entailed by a flexural deformation of non rectilinear extrudates. Indeed, geometrical irregularities are inevitably produced when shaping by extrusion and drying. Irregular geometries (slightly curved samples) can explain that a displacement of few micrometers is necessary to change from punctual contact to line contact after local material crushing. The importance of slight imperfections on the contact status is also pointed out by [20] on granular aggregates and by [33] on sand particles.

Hence, the main discrepancies between numerical and experimental results may be due to geometrical factors (shape and roughness of small cylinders). In order to adjust Drucker-Prager criterion parameters on experimental results, the experimental displacements have to be corrected such that the initial position of the platen is shifted in order to correspond to the stabilized contact. The specimen chosen for the comparison is representative of the average behavior and does not show large brittle events. A comparison of numerical and experimental load-displacement curves is plotted in Figure 8 with adjusted parameters $\sigma_c = 19$ MPa and $\beta = 15°$. The correlation of the yielding load and of the hardening is good for this specimen. The experimental dispersion of the yielding load leads to an estimation of the compressive yields stress of $\sigma_c = 19$ MPa ± 3 MPa. The identification of the friction angle β is less precise because of the strong uncertainty on the hardening slope.

Following the same methodology, the compressive yield strength of the second lot of extrudates is adjusted to $\sigma_c' = 29$ MPa thanks to the tests on the groove at 40 deg. The second lot of extrudates is less porous and more resistant than the first lot. The simulations of the tests with other groove angles, conducted with the strength criterion identified at 40 deg, show a good agreement with the experimental characteristic failure loads, Figure 9. The increase of the crushing strength with the platen angle was also obtained with a *Discrete Elements Model* by [20].

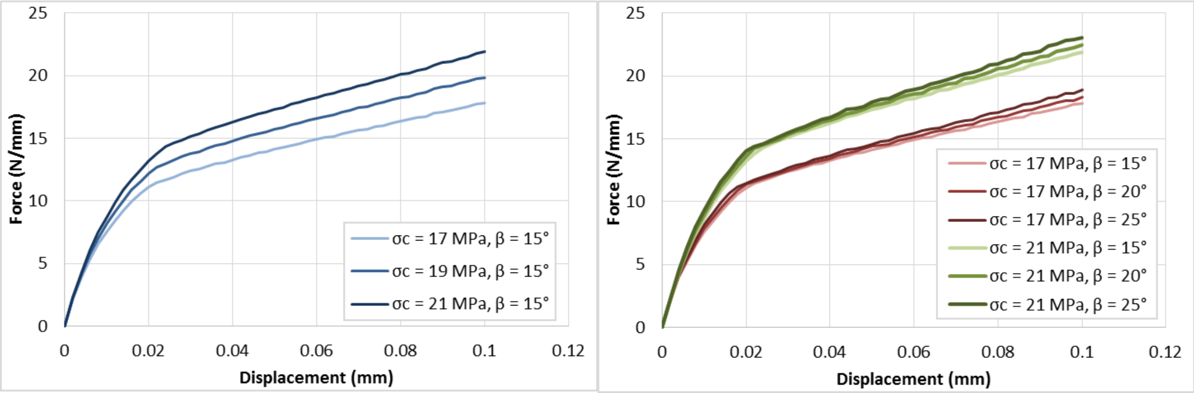

Figure 7: Numerical results, influence of internal friction angle β and yield strength under compression σ_c on the numerical load-displacement curve

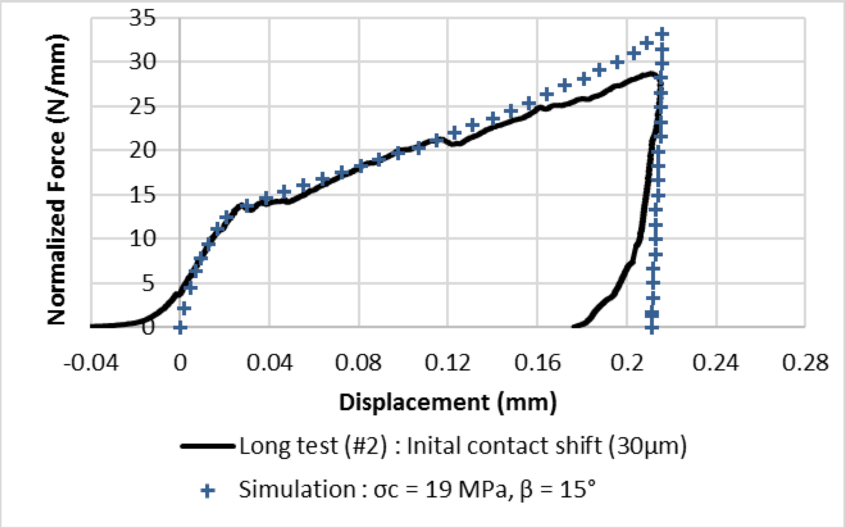

Figure 8: Comparison of numerical and experimental load-displacement curves of multi-points crushing test (groove angle of 40 deg, 1st lot of extrudates). The experimental displacement is shifted by -30µm to discard initial contact due to surface roughness

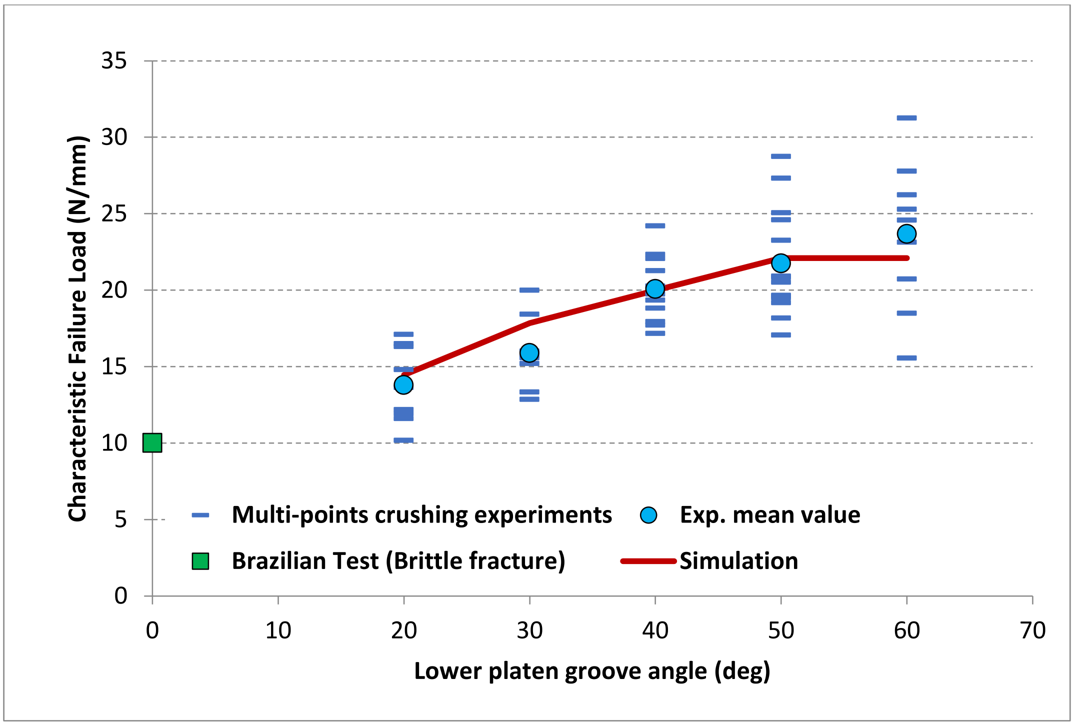

Figure 9: Comparison of numerical and experimental characteristic failure loads of multi-points crushing test at various groove angles (2^{nd} lot of extrudates). The experimental mean fracture load of the Brazilian test (no groove) is indicated as a reference for brittle fracture strength.

3.2.2 Evolution of plastic strain field

Figure 10 shows the evolution of the equivalent plastic strain field, ε_{eq}^{pl}, at different stages of the test. The strain scale is limited at 1% to better illustrate the propagation of the plastic zones (in brown). Plastic strain first appears under each contact surface (stage ①). While these zones grow and remain unconnected, the apparent stiffness remains high. Then, the plastic zones merge and the apparent stiffness drops (stage ②). A plastic band appears under combined compression and shear stresses in the specimen. The shape of the band and the load at which it appears do not depend on the mesh size. Finally, a unique plastic zone keeps growing, resulting in a linear hardening behavior (stage ③). In these stages, the equivalent plastic strain field has close similarities with the fracture morphology observed experimentally, as illustrated in Figure 5 and Figure 6. The increase of the apparent stiffness at the end of the loading phase (stage ④) can be explained by a geometrical effect due to large deformations of the specimen.

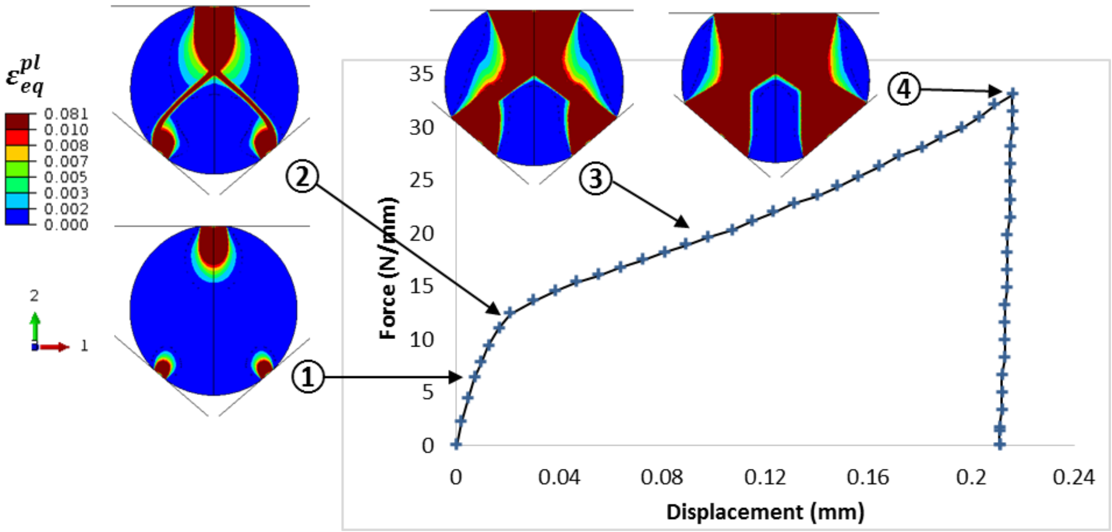

Figure 10: Evolution of the equivalent plastic strain inside the sample at different stages of the multi-points crushing test

3.2.3 Mass of damaged material

Masses of damaged material are estimated from the numerical model, based on the plastic energy dissipation. Only the plastic dissipation is taken into account. For a given threshold of dissipation density, the corresponding plastic area (2D) is extracted, then multiplied by the material mass density and by the total length of the specimens. Different dissipation thresholds are considered: E_{diss}^{pl}>0, >0.25, >1 and >3 mJ/mm^3. The calculated masses are then compared with the experimental masses of fines and coarse fragments, measured for short and long tests, as a function of the dissipated energy (see Figure 11). The graphic confirms that the estimated masses of damaged material are of the same order of magnitude as the experimental masses of fragments. The mass of fine fragments approximately corresponds to the volume subjected to a plastic dissipation density higher than 3 mJ/mm^3: it is almost zero for short tests as the total dissipated energy is low, and strongly increases for long tests with a higher dissipation. The total mass of fragments, including fine and coarse ones, appears to be less correlated with a plastic dissipation threshold: it corresponds to a plastic dissipation density lying between 0.25 and 1.0 mJ/mm^3.

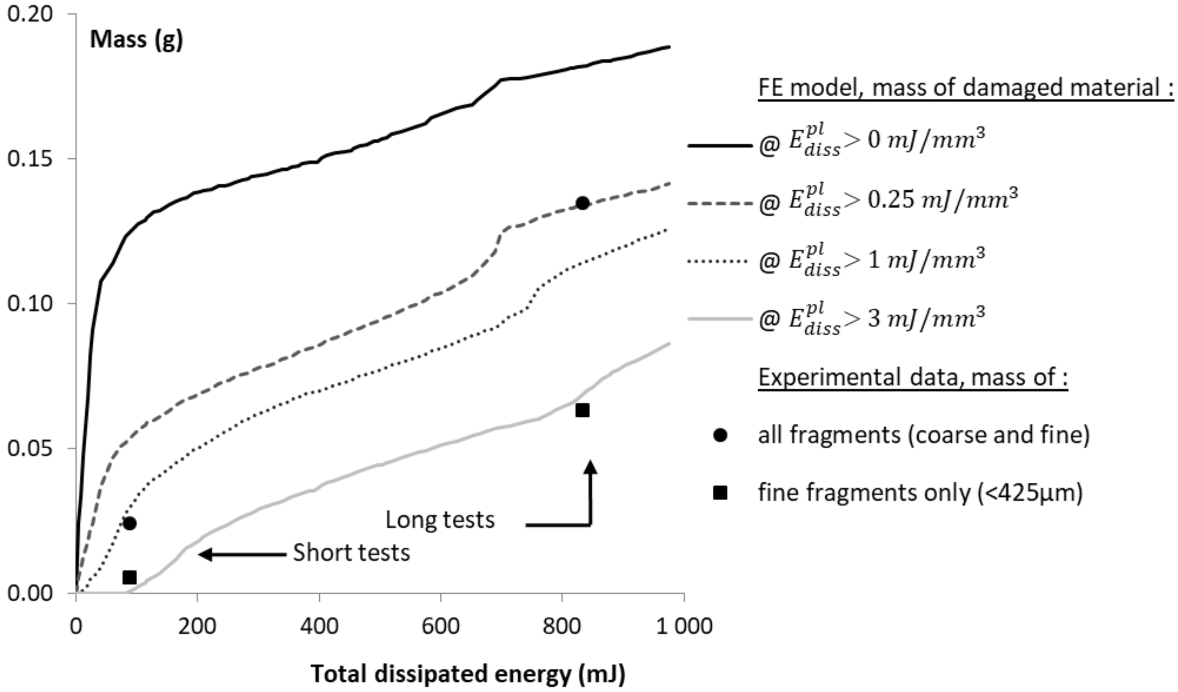

Figure 11: Comparison of numerical masses of damaged material with experimental masses of fragments as a function of the dissipated energy.

3.3 Discussion on the representation of ductile damage by a plastic model

The Drucker-Prager criterion is well adapted to represent the fracture strength of catalyst supports if densification is neglected [16]. However, post-fracture behavior is more complex to represent than the fracture strength because it depends on the damage mechanisms and, jointly, on stress triaxiality. Previous studies have shown the behavior of catalyst supports is mainly brittle under uniaxial compression, whereas irreversible strains are obtained under multiaxial compression [34]. Densification is highly suspected under very high hydrostatic pressures, as observed on other porous alumina under iso-static pressing [35,36]. Damage and deformation mechanisms are difficult to observe when taking place at the scale of pores and alumina crystallites aggregates. Macroscopic consequences are easier to describe. For instance, irreversible deformation can be the consequence of micro-cracking and frictional sliding between crystallites aggregates. In the multi-point crushing test, the multi-axial compression state leads to multiple damage intensities. As a consequence, several mechanisms are observed: irreversible deformation, micro-cracks, fragmentation, and ultimately macro cracks. Associated with the Drucker-Prager criterion, a perfectly plastic flow is chosen to model a ductile behavior. After adjustment of the internal friction angle β and the yield strength σ_c, this model mimics fairly well the damageable behavior of the specimen under the multi-point crushing test. The morphology of the plastic strain field has close similarities with the fracture morphology observed experimentally. The volume of material undergoing a plastic dissipation density higher than 3 mJ/mm^3 approximately corresponds to the volume of fine fragments generated during the tests. The model thus helps to interpret the test and to draw a damaging scenario. The plastic dissipation density or – almost equivalently – the equivalent plastic strain, is interpreted as an indicator of the size of the fragments. For low dissipation (< 0.25mJ/mm^3), the material is damaged by micro-cracking without production of fragments. As energy dissipation increases (from 0.25 to

3 mJ/mm^3), micro-cracks coalesce, leading to the production of coarse fragments. At higher dissipations, both coarse and fine fragments are produced.

4 Conclusions

The multipoint crushing test carried out on highly porous γ-alumina reveals the damageable behavior of catalytic supports under multi-axial compressive state. Multiple macroscopic consequences of damage mechanisms are observed: irreversible deformation, fragmentation, and ultimately macro cracks. A Drucker-Prager criterion has been adjusted to reproduce the global behavior of the specimen under the multi-point crushing test. A local plastic dissipation density of 3mJ/mm^3 is well correlated with the region of fragmentation (<450µm). This model is thus able to represent global ductile damage likely produced at small scale by local brittle micro-cracks or frictional sliding between crystallites aggregates at the nano-scale. Further investigations are necessary to better understand the nature of the damage at small scale and then to improve the physical model. Nano-indentation tests are undertaken to assess the damageable mechanical behavior at such scales [37]. Complementary observations, thanks to Focused Ion Beam micrography (FIB-SEM) [38] or high resolution X-ray micro-tomography [39], may be used to look for cracks at early stages of damage. The industrial stake is to improve the material strength, still keeping pure alumina at a porosity rate higher than 70% and to design catalytic reactors with no risk of catalyst supports fragmentation.

5 Acknowledgments

The study was entirely funded by *IFP Energies nouvelles*. The authors thank the teams of the *Powder Materials Engineering Department* of *IFPEN* for preparing the samples and the *Material Characterization Department* for their grateful help, especially M. Denis Roux for the mechanical tests and granulometry, and M. Florent Moreau for the SEM fractography.

6 References

[1] J. Verstraete, D. Guillaume, M. Roy Auberger, Catalytic Hydrotreatment and Hydroconversion: Fixed Bed, Moving Bed, Ebullated Bed and Entrained Bed, in: A.-Y. Huc (Ed.), Heavy Crude Oils - From Geology to Upgrading, an Overview, Editions Technip, 2011.
[2] D. Wu, L. Song, B. Zhang, Y. Li, Effect of the mechanical failure of catalyst pellets on the pressure drop of a reactor, Chemical Engineering Science 58 (2003) 3995–4004.
[3] ASTM D32 Committee, Test Method for Determination of Bulk Crush Strength of Catalysts and Catalyst Carriers, ASTM International, West Conshohocken, PA, 2018.
[4] Y. Li, X. Li, L. Chang, D. Wu, Z. Fang, Y. Shi, Understandings on the scattering property of the mechanical strength data of solid catalysts, Catalysis Today 51 (1999) 73–84.
[5] Y. Li, D. Wu, J. Zhang, L. Chang, D. Wu, Z. Fang, Y. Shi, Measurement and statistics of single pellet mechanical strength of differently shaped catalysts, Powder Technology 113 (2000) 176–184.
[6] D. Wu, J. Zhou, Y. Li, Mechanical strength of solid catalysts, AIChE J. 53 (2007) 2618–2629.
[7] T. Rouxel, Mechanical Properties of Ceramics, in: P. Boch, J.-C. Niepce (Eds.), Ceramic Materials, ISTE, London, UK, 2007, pp. 261–324.

[8] A.A. Griffith, The Phenomena of Rupture and Flow in Solids, Philosophical Transactions of the Royal Society A: Mathematical, Physical and Engineering Sciences 221 (1921) 163–198.

[9] M.F. Kanninen, C.H. Popelar, Advanced fracture mechanics, Oxford University Press; Clarendon, New York, Oxford, 1985.

[10] ASTM D32 Committee, Test Method for Single Pellet Crush Strength of Formed Catalysts and Catalyst Carriers, ASTM International, West Conshohocken, PA, 2017.

[11] M.F. Ashby, C.G. Sammis, The damage mechanics of brittle solids in compression, PAGEOPH 133 (1990) 489–521.

[12] S. Meille, M. Lombardi, J. Chevalier, L. Montanaro, Mechanical properties of porous ceramics in compression: On the transition between elastic, brittle, and cellular behavior, Journal of the European Ceramic Society 32 (2012) 3959–3967.

[13] D. Staub, S. Meille, V. Le Corre, J. Chevalier, L. Rouleau, Revisiting the Side Crushing Test Using the Three-Point Bending Test for the Strength Measurement of Catalyst Supports, Oil Gas Sci. Technol. – Rev. IFP Energies nouvelles 70 (2015) 475–486.

[14] J.W.L. Beeckman, N.A. Fassbender, T.E. Datz, M. Cunningham, D.L. Mazzaro, Predicting Catalyst Extrudate Breakage Based on the Modulus of Rupture, Journal of visualized experiments JoVE (2018).

[15] J.W.L. Beeckman, M. Cunningham, N.A. Fassbender, T.E. Datz, Length-to-Diameter Ratio of Extrudates in Catalyst Technology, Chem. Eng. Technol. 40 (2017) 1844–1851.

[16] D. Staub, S. Meille, V. Le Corre, L. Rouleau, J. Chevalier, Identification of a damage criterion of a highly porous alumina ceramic, Acta Materialia 107 (2016) 261–272.

[17] B.R. Lawn, Indentation of Ceramics with Spheres, Journal of the American Ceramic Society 81 (1998) 1977–1994.

[18] P. Clément, S. Meille, J. Chevalier, C. Olagnon, Mechanical characterization of highly porous inorganic solids materials by instrumented micro-indentation, Acta Materialia 61 (2013) 6649–6660.

[19] D.C. Drucker, The continuum theory of plasticity on the macroscale and the microscale, J.Mater. 1 (1966) 873–910.

[20] R. Artoni, A. Neveu, Y. Descantes, P. Richard, Effect of contact location on the crushing strength of aggregates, Journal of the Mechanics and Physics of Solids 122 (2019) 406–417.

[21] M. Raous, L. Cangémi, M. Cocu, A consistent model coupling adhesion, friction, and unilateral contact, Computer Methods in Applied Mechanics and Engineering 177 (1999) 383–399.

[22] F. Perales, S. Bourgeois, A. Chrysochoos, Y. Monerie, Two field multibody method for periodic homogenization in fracture mechanics of nonlinear heterogeneous materials, Engineering Fracture Mechanics 75 (2008) 3378–3398.

[23] C. Daux, N. Mos, J. Dolbow, N. Sukumar, T. Belytschko, Arbitrary branched and intersecting cracks with the extended finite element method, Int. J. Numer. Meth. Engng. 48 (2000) 1741–1760.

[24] J. Dolbow, N. Moës, T. Belytschko, An extended finite element method for modeling crack growth with frictional contact, Computer Methods in Applied Mechanics and Engineering 190 (2001) 6825–6846.

[25] A. Neveu, R. Artoni, P. Richard, Y. Descantes, Fracture of granular materials composed of arbitrary grain shapes, Journal of the Mechanics and Physics of Solids 95 (2016) 308–319.

[26] D. Jauffrès, C.L. Martin, A. Lichtner, R.K. Bordia, Simulation of the toughness of partially sintered ceramics with realistic microstructures, Acta Materialia 60 (2012) 4685–4694.

[27] P. Euzen, P. Raybaud, X. Krokidis, H. Toulhoat, J.-L. Le Loarer, J.-P. Jolivet, C. Froidefond, Alumina, in: F. Schüth, K.S.W. Sing, J. Weitkamp (Eds.), Handbook of Porous Solids, Wiley-VCH Verlag GmbH, Weinheim, Germany, 2002, pp. 1591–1677.

[28] M. Digne, Alumina Supports, in: H. Toulhoat, P. Raybaud (Eds.), Catalysis by transition metal sulphides: From molecular theory to industrial application, Technip, Paris, France, 2013.

[29] Abaqus (Ed.), ABAQUS Documentation, version 6.14, Providence, RI, USA, 2014.

[30] M. Arnold, A.R. Boccaccini, G. Ondracek, Prediction of the Poisson's ratio of porous materials, Journal of Materials Science 31 (1996) 1643–1646.

[31] J. Sanahuja, L. Dormieux, S. Meille, C. Hellmich, A. Fritsch, Micromechanical Explanation of Elasticity and Strength of Gypsum, J. Eng. Mech. 136 (2010) 239–253.

[32] A. Bouterf, J. Adrien, E. Maire, X. Brajer, F. Hild, S. Roux, Identification of the crushing behavior of brittle foam, Journal of the Mechanics and Physics of Solids 98 (2017) 181–200.

[33] M.C. Todisco, W. Wang, M.R. Coop, K. Senetakis, Multiple contact compression tests on sand particles, Soils and Foundations 57 (2017) 126–140.

[34] D. Staub, Étude du comportement mécanique à rupture des alumines de forte porosité: Application aux supports de catalyseurs d’hydrotraitement des résidus. Thèse de doctorat, Lyon, 2014.

[35] Y.B.P. Kwan, D.J. Stephenson, J.R. Alcock, The porosity dependence of flexural modulus and strength for capsule-free hot isostatically pressed porous alumina, Journal of Materials Science 35 (2000) 1205–1211.

[36] T. Ostrowski, J. Rödel, Evolution of Mechanical Properties of Porous Alumina during Free Sintering and Hot Pressing, Journal of the American Ceramic Society 82 (1999) 3080–3086.

[37] M. Moula, S. Meille, V. Le Corre, J. Chevalier, Mechanical characterization of meso-porous alumina by micro- and nano-indentation, Materials Today Communications 25 (2020) 101315.

[38] Z. Chen, X. Wang, F. Giuliani, A. Atkinson, Fracture Toughness of Porous Material of LSCF in Bulk and Film Forms, Journal of the American Ceramic Society 98 (2015) 2183–2190.

[39] A. Bouterf, E. Maire, S. Roux, F. Hild, X. Brajer, E. Gouillart, E. Boller, Analysis of compaction in brittle foam with multiscale indentation tests, Mechanics of Materials 118 (2018) 22–30.